JUSTC

Article

http://justc.ustc.edu.cn

Received: November 14, 2023; Accepted: February 01, 2024

The effects of low-velocity layer and basin topography in near-field ground motion amplification

Zeyu Lu[1], Jian Wen[1,2], and Feng Hu[1,2] ✉

[1]*School of Earth and Space Sciences, University of Science and Technology of China, Hefei 230026, China;*
[2]*Mengcheng National Geophysical Observatory, University of Science and Technology of China, Mengcheng 233500, China*

✉Correspondence: Feng Hu, Feng Hu, E-mail: hufeng07@ustc.edu.cn

Graphical abstract

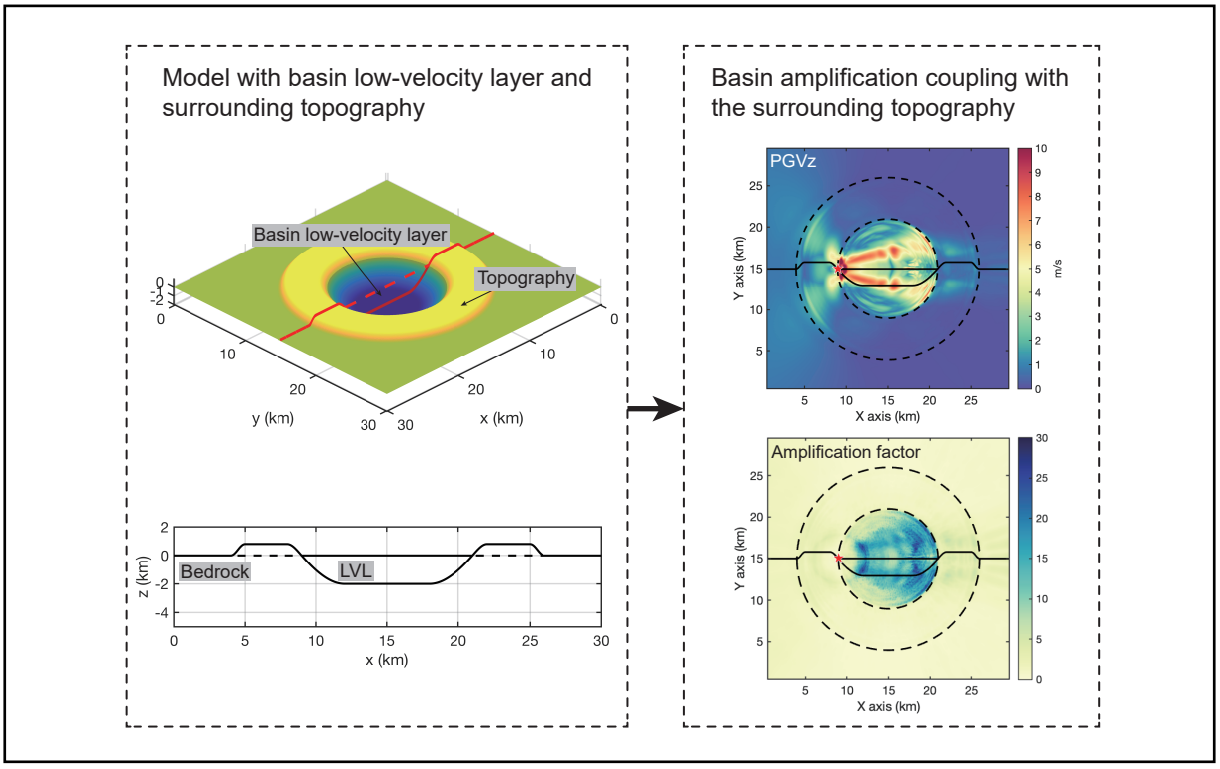

By introducing a basin model that includes both low-velocity layer and topography in earthquake ground motion simulation, the characteristics of ground motion amplification can be acquired.

Public summary

- The effect of the low-velocity layer in contrast with the surrounding mountain topography of a sedimentary basin model is scrutinized by near-field ground motions.
- Velocity contrast between bedrock and low-velocity layer plays a pivotal role in controlling the amplitude of the ground motion amplification.
- Amplification caused by the topography mainly spreads along the mountain edge and may interact with the low-velocity layer to amplify ground motion.

Citation: Lu Z Y, Wen J, Hu F. The effects of low-velocity layer and basin topography in near-field ground motion amplification. *JUSTC*, **2024**, 54(0): . DOI: 10.52396/JUSTC-2023-0156

JUSTC

Article

http://justc.ustc.edu.cn

Received: November 14, 2023; Accepted: February 01, 2024

The effects of low-velocity layer and basin topography in near-field ground motion amplification

Zeyu Lu[1], Jian Wen[1,2], and Feng Hu[1,2] ✉

[1]*School of Earth and Space Sciences, University of Science and Technology of China, Hefei 230026, China;*
[2]*Mengcheng National Geophysical Observatory, University of Science and Technology of China, Mengcheng 233500, China*

✉Correspondence: Feng Hu, Feng Hu, E-mail: hufeng07@ustc.edu.cn

Cite This: *JUSTC*, **2024**, 54(X): (11pp)

Read Online

Abstract: Near-field ground motion amplification at sedimentary basins is widely observed and crucial to the earthquake hazard assessment. However, the effect of basin topography coupling with the low-velocity layer (LVL) in the ground motion amplification is yet to be fully understood. By constructing 3D basin models with surrounding mountain terrains and performing ground motion simulations, we compare the ground motion characteristics with different basin LVL depths and LVL velocities. The velocity contrast between LVL and bedrock controls the amplification magnitude. The maximum amplification area in the model changes from the central part to the periphery part of the basin with the velocity contrast decreasing and can be greatly influenced by the distance between the source and the basin. Amplification also spreads along the mountain edge circling the basin. Our work sheds light on the distribution of amplification within sedimentary basins surrounded by mountains, revealing that the velocity contrast between the LVL and bedrock plays a pivotal role in controlling the magnitude of amplification.

Keywords: low-velocity layer; basin topography; strong ground motion

CLC number: P315.3$^+$1 **Document code:** A

1 Introduction

Near-field ground motion amplification in basin areas is substantial to earthquake hazard assessment. This is particularly pertinent due to the occurrence of numerous destructive earthquakes in proximity to basins, such as the 1994 Northridge earthquake in the Los Angeles basin area, the 1995 M6.9 Kobe, Japan earthquake in the Osaka basin, the 2008 M7.9 Wenchuan earthquake and the 2021 M6.0 Luxian earthquake in the Sichuan basin area[1–5]. The amplified amplitude of ground motion and longer lasting time of seismograms are the key characteristics in basin areas. However, the effect of the topography of the basin area coupling with the effect of the low-velocity layer in the basin is yet to be fully elucidated.

Previous studies have yielded a wealth of analytical and numerical findings, such as layered models or simple basin models in the homogeneous half-space[6–8]. The numerical methods are introduced to the solution of more complicated basin geometries or media. Studies have employed 2-dimensional models, considering the joint of semi-elliptical and rectangle, and half-cosine configurations[9]. Plane-incident waves are frequently applied for some of these works. Three-dimensional models are also involved in previous studies, such as semi-ellipsoidal, hemispherical, and trapezoidal[10–13]. Researchers also conducted ground motion simulations on real basins, such as the Seattle basins, the Indo-Gangetic (IG) basin, the Kinburn basin, the Beijing basin, the Taipei basin, and the Sichuan basin[2, 14–22].

Basins are typically enclosed by mountains. The topography effect also plays a role in contributing to the seismic waveform complexities, which have been known for decades[23–27]. Numerical methods are also applied to study the topographic site effects, although many of them have focused on 2D simulations[28–30]. Some studies simultaneously consider the effects of topography and velocity structure on seismic ground motion and amplification[30–32]. However, due to the complexity of real velocity structures and topography, assessing seismic responses can be challenging[28, 31, 33]. Thus, we propose an investigation into the contributions of both factors to the ground motion amplification within a set-up 3D model.

Among the existing studies, a systematic analysis of basin depth coupling with basin topography within 3D scenarios has been lacking. For instance, models featuring depth-dependent, wedge-shaped models have not been considered. To address the gap, we start with a baseline model, the sedimentary basin depth and the velocity contrast between the low-velocity layer and the bedrock are discussed. To isolate the effect of basin topography in contrast to the low-velocity layer of the sedimentary basin, we scrutinize the basin amplification effect by comparing a basin model with a homogeneous half-space model. Furthermore, the wedge-shaped basin model is also discussed.

2 Models and methods

2.1 3D sedimentary basin geometry

We aim to establish a three-dimensional basin model that can

DOI: 10.52396/JUSTC-2023-0156
JUSTC, **2024**, 54(X):

be characterized by parameters to conduct near-field seismic ground motion simulation. Ayoubi et al. systematically analyzed the 2D basin models' ground motion characteristics using the finite-element method[9]. They proposed two types of models: semi-elliptical and half-cosine 2D basin models to perform simulation. We integrate the half-cosine method from Ayoubi et al. with cubic-spline interpolation to define the basin geometry. The basin area is bounded by encircling mountains. The mathematical expression of the central line curve is given by Eq. (1), which controls the 3D model boundaries in the x-axis plane.

$$p(x)=\begin{cases} -d, & |x|\leqslant a/2; \\ B_{i1}x^3+B_{i2}x^2+B_{i3}x+B_{i4}, & a/2<|x|\leqslant a+b; \\ h, & a+b<|x|\leqslant a+b+w; \\ \dfrac{h}{2}\cos\left[\dfrac{\pi}{b}(x-a-b-w)\right]+\dfrac{h}{2}x, & a+b+w<|x|\leqslant a+2b+w; \\ 0, & |x|\geq a+2b+w. \end{cases} \tag{1}$$

where parameters a, b, h, d, and w are topography and basin geometry constraining parameters, which represent the radius of the basin, the width of the transition area, the height of the mountain around the basin, the depth of the sedimentary basin and the width of the mountain around the basin, respectively (Table 1). A schematic diagram of the definitions of these parameters is shown in Fig. 1c and 1d. In the model with fixed depth, by rotating this curve around a central axis to form a three-dimensional surface, the concave portions in the central part of the surface are filled with low-velocity media, forming a low-velocity sedimentary basin (Fig. 1a, 1c). This model is similar to the model in Ayoubi et al. and Qin et al. [9,11], but includes the mountains around the basin.

We also designed the wedge-shaped basin model. In the wedge-shaped basin model, The model is constructed based on the x-direction central line, employing the same interpolation method in the y-direction as that used to derive the central axis, forming the entire plane (Fig. 1b, d). Similarly, the concave portions in the central part of the surface, which lie below the ground surface, are filled with low-velocity media, forming a sedimentary basin.

2.2 Numerical modeling

The ground motion simulations are performed using the CGFD3D (Curved Grid Finite-Difference 3D) code, which applies 3D collocated-grid finite-difference code to solve the velocity-stress equations for the curvilinear grid[34]. In this method, the fourth-order Runge-Kutta scheme is applied to update the wavefield, and the DRP/opt MacCormack scheme provides a fourth-order accuracy in space[35]. With a 3D curve grid, the grid can align with the surface topography and avoid spurious diffusion. The code is verified in the work of Zhang et al. by comparison against GRTM (generalized reflection/transmission coefficients method) and SpecFEM3D code and shows good consistency with the reference solution [34, 36, 37].

V_s, V_p, and ρ represent the shear wave velocity, the compression wave velocity, and the density, respectively. In models with a low-velocity layer (LVL), the basin area is filled with a low-velocity material with a given depth d. In all models, the shear wave velocity of the bedrock is consistently set at 3000 m/s. All models assume a Poisson medium to constrain the relationship between P-wave velocity and S-wave velocity. The density for specific velocity is constrained by the empirical relationship of Brocher[38]. With the range of 1500 m/s < V_p < 8500 m/s, the relation between V_p and density ρ is described in Eq. (2).

$$\rho(\mathrm{g/cm^3})=1.6612V_p-0.4721V_p^2+0.0671V_p^3-0.0043V_p^4+0.000106V_p^5. \tag{2}$$

All models have a horizontal grid size of 50 m to ensure computational accuracy and reduce numerical dispersion. To reduce the computational burden, the vertical grid size gradually varies from 50 m near the surface to 100 m in the deeper regions. The simulation is performed using a time interval of 0.003 s. Among all groups of simulations, the lowest S-wave velocity is 1500 m/s, considering a minimum PPW (points per minimum wavelength) of 8, the wave field can provide a reliable frequency of up to 3.75 Hz. The size of the model is 30 km × 30 km × 12 km and the grid points within the simulation area are 600 × 600 × 90. A total of 144 cores on a cluster are used for the simulation.

2.3 Ground motion amplification evaluation

The ground motion amplification is evaluated with peak ground velocity (PGV), peak ground acceleration (PGA), and amplification factor. Regarding the amplification factor, we

Table 1. Basin model parameters definition and baseline values.

Parameter	Definition	Baseline value
a	The radius of the basin	6000 m
b	Width of the transition area	1000 m
h	Height of the mountain around the basin	800 m
d	Depth of the fixed-depth flat basin model	Change as demand
d_1,d_2	Depth of the wedge-shaped basin model on two sides	Change as demand
w	Width of the mountain	3000 m
V_p	Compression wave velocity	Change as demand
V_s	Shear wave velocity	Change as demand
ρ	Density	Change as demand

DOI: 10.52396/JUSTC-2023-0156
JUSTC, **2024**, 54(X):

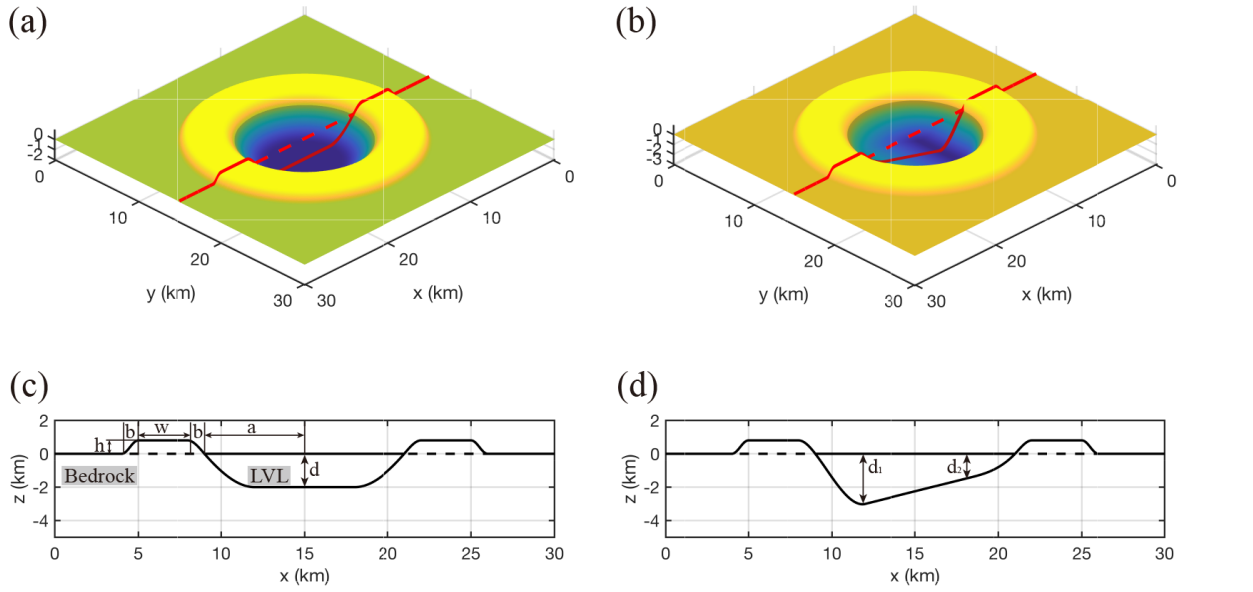

Fig. 1. Basin model geometry. Three-dimensional basin geometry for (a) fixed-depth basin model and (b) wedge-shaped basin model, where the subsurface concave regions are filled with low-velocity media. The cross-section of the central red lines in (a) and (c) are shown in figures (c) and (d). The geometric parameters of the basin are labeled in Figures 1(c) and 1(d), whose definitions are listed in Table 1. In the following ground surface images in this article, the geometric cross-section of the basin is depicted in the center of the images.

followed the approach of Wirth et al. but made some modifications to achieve a smoother graphical representation[14]. The following procedure is applied to calculate the amplification factor on the ground surface: Start with the low-pass filtered velocity seismogram at each grid point $v(t;x,y)$, we perform a Fourier transform to the filtered waveform to get the amplitude spectrum $F(\omega;x,y)=\mathcal{F}[v(t;x,y)]$. The reference model's ground motion is calculated with a half-space homogeneous model, whose amplitude spectrum $F_{\mathrm{ref}}(\omega;x,y)=\mathcal{F}[v_{\mathrm{ref}}(t;x,y)]$ is also calculated. The amplification factor γ is defined as

$$\gamma(x,y)=\frac{\max[F(\omega;x,y)]}{\max[F_{\mathrm{ref}}(\omega;x,y)]}. \tag{3}$$

For each grid point, we can have the amplification factor $\gamma(x,y)$ and the corresponding $\omega_{\max}$. Through this method, we can have spectral ratios of basin amplification relative to the reference model. By dividing the maximum of the reference model amplitude spectrum, we can eliminate the effects of source radiation patterns and geometric spreading, allowing for a more accurate evaluation of the influence of topography and low-velocity layers on ground motion. This helps to minimize the effect of single-station local errors and to find the maximum amplification among different frequencies[39]. The amplification factor in this work is calculated using the z-component velocity seismogram.

The reason for modifying the approach of Wirth et al. is that we have found, in models with sharp velocity boundaries, that results obtained through comparing amplitude spectra at a fixed frequency exhibit spatial discontinuities. Comparing the maximum values of the amplitude spectra provides a smoother representation of the model. Due to variations in model and seismic source configurations across different studies, the amplification factor obtained through this method can only be compared within the scope of this study. The result is internally consistent and they can reflect the amplification characteristics.

3 Results

3.1 Overall characteristics of ground motion

To understand the effect of the low-velocity layer on the ground motion amplification, we filled low-velocity material within the basin area. This baseline model LVL has a V_s velocity of 1500 m/s, compared to a bedrock V_s velocity of 3000 m/s. With all other parameters constant with the baseline parameter. We apply a simple dislocation source at (9000 m, −15000 m, −1000 m). The moment is 1.23e18 Nm, corresponding to ~Mw 6.0. For the source, the strike dip and rake are 0 degrees, 45 degrees, and 90 degrees, respectively. In subsequent simulations, we applied the same source configuration. The velocity seismograms on the ground are subjected to a low-pass filter with a cutoff frequency of 3.75 Hz, then the amplification factor is calculated.

A source time function of the Ricker wavelet is applied with a central frequency f_c of 2 Hz and time shift t_0 of 0.7 s. With a basin depth d of 1000 m, the ground motion snapshot is shown in Fig. 2. The result shows that the seismic waves keep oscillating inside the basin area, especially near the boundary area. Upon reaching the far end of the basin, seismic waves reflect due to velocity contrasts and return to the interior part of the basin. This oscillatory process repeats continuously, resulting in a larger amplitude and longer duration of ground motion within the low-velocity region.

The distribution of the maximum PGVz and PGVh values (Fig. 3a, 3b) is related to the radiation pattern of the reverse fault dislocation source we applied. As shown in Fig. 3a, the amplification extends in a V-shaped pattern within the basin. While on the west side of the source, the V-shaped pattern is

DOI: 10.52396/JUSTC-2023-0156
JUSTC, **2024**, 54(X):

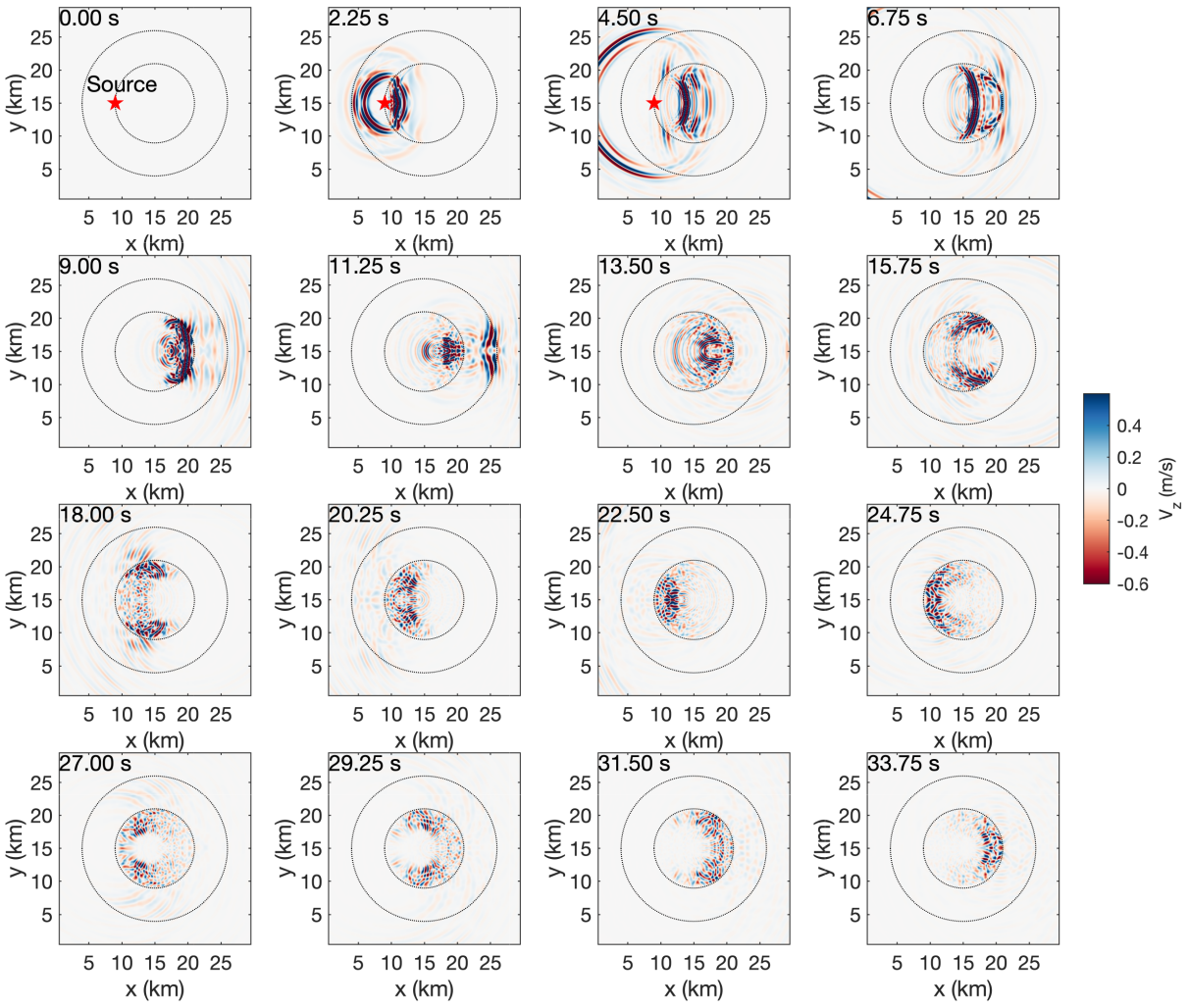

Fig. 2. Z-component velocity snapshot at the ground surface of the fixed-depth baseline model.

obstructed by the topography and has a narrower distribution compared to the east side covered by LVL. On the western edge of the mountain range, ground motion amplification caused by changes in topography can be observed, mainly on the boundary of the mountain. A more distinct block-like distribution is observed in PGVh compared to PGVz (Fig. 3b). Compared to the distribution of PGV, the distribution of the amplification factor can illustrate the boundary of the LVL. In this baseline model, regions with stronger amplification are present in the middle of the basin (Fig. 3c). Fig. 4a shows the 3-component seismogram at receiver line 1, and a Z-shaped pattern of repetitive ground motion can be observed. Because the central part between the red lines of line 1 is located within the low-velocity region, their intensity is significantly higher than that of the receivers outside the basin. Fig. 4b shows the 3-component seismograms at receiver line 2. The strongest amplification occurs at a few seconds after the seismic wave enters the basin, however, the oscillation inside the basin can last a very long time, especially at the points near the basin boundary. The oscillation is weaker at the center of the basin.

3.2 Effect of LVL depth

To understand the effect of the low-velocity layer on the ground motion amplification, we filled low-velocity material within the basin area. With all other parameters constant with the baseline parameter, we investigate 3 different scenarios, with the basin depth d changes from 1000 m to 2000 m with an interval of 500 m. The seismic source configuration is the same as in the previous section.

The amplification factor reveals a stronger amplification within the LVL zone, especially within the flat area of the LVL (Fig. 5a, 5b, 5c). Compared with the half-space homogeneous reference model, the basin exhibits two regions with more pronounced amplification values within the LVL zone. The first peak is located in the transitional zone between the flat and slope part of the basin and represents a circle, close to the source. It is related to the pattern of the homogeneous half-space model reference result used to calculate the amplification factor. Besides this, the amplification primarily occurs on the far side of the basin, with an amplification factor of 20 to 30 compared to the reference model.

The maximum PGV values decrease with the increasing LVL depth (Fig. 5d, 5e, 5f). The number of PGV local peaks within the basin area decreases from 4 groups to 1 group as the basin depth increases from 1000 m to 2000 m. This phenomenon may indicate a reduction in the number of multiple

DOI: 10.52396/JUSTC-2023-0156
JUSTC, **2024**, 54(X):

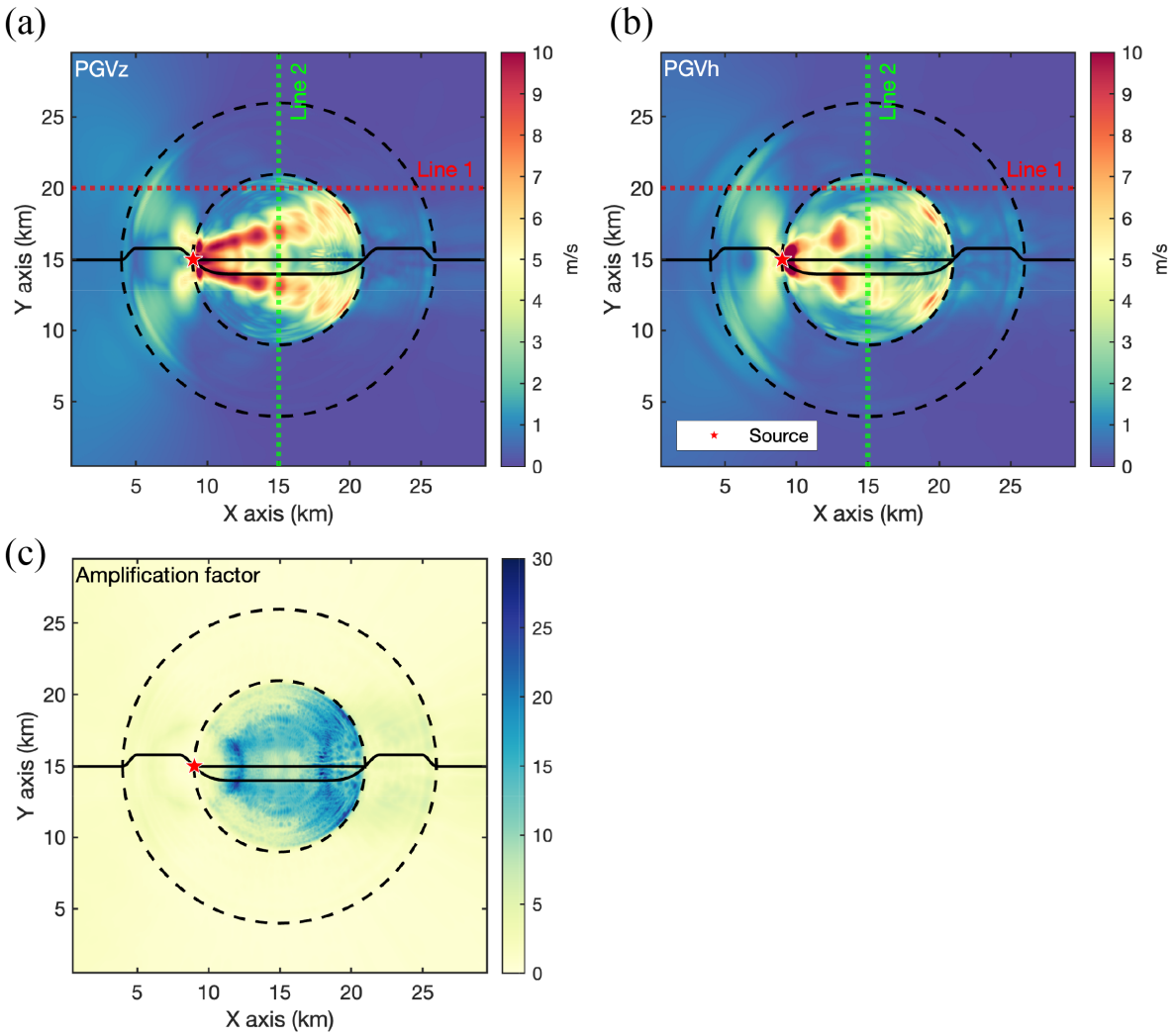

Fig. 3. (a) PGVz, (b) PGVh, and (c) amplification factor of the fixed-depth baseline model at the ground surface. In Figures (a), (b), and (c), the dashed circle shows the boundary of LVL and topography. The central section profile is drawn in the center of the plot with a solid black line. The dashed red line and green line in Figures (a) and (b) represent two lines of receivers.

reflections within the basin. Thus, we infer that basin depth is not the primary factor influencing the degree of amplification within the basin, but it does alter the distribution pattern of amplification within the basin.

3.3 Effect of LVL velocity

The shear wave velocity of the bedrock below the basin topography is 3000 m/s. By changing the medium velocity within the sediment basin from 1500 m/s to 3000 m/s with an interval of 500 m/s, we investigate 4 different scenario cases and show the amplification factor and PGVz in Fig. 6. Generally, the absence of LVL controls the amplification behavior. The strongest amplification without the source area occurs at the far end of the basin. The magnitude of the velocity contrast directly controls the magnitude of the amplification factor. With the increase of the LVL velocity, the amplification decreases. A speed contrast of 1500 m/s leads to a maximum amplification factor of ~30.

Apart from the significant amplification of ground motion within the basin, the basin acts as a kind of "lens" causing waves to focus as they pass through the basin, resulting in a V-shaped pattern of increased ground motion that persists beyond the LVL zone. This demonstrates that the energy originating from the source is still more concentrated than the reference model even after passing through the basin. As the velocity contrast diminishes, this phenomenon of wavefront focusing weakens, and the opening of the V-shape gradually widens until it disappears.

As the velocity contrast diminishes, the result shows that the locations with stronger amplification within the basin shift from the central flat region of the basin to the areas on either side of the basin. The central region of the basin exhibits a higher peak when the first arrivals of waves reach it, and the level of amplification depends on the strength of the transmitted and reflected waves upon their initial entry into the basin. However, reflected waves on the opposite side of the basin primarily propagate back and forth around the perimeter of the basin, possibly due to the thinner transitional zones around the periphery, resulting in more pronounced multiple reflections. As the velocity contrast varies, there is a change in the balance between the first arrivals and subsequent mul-

DOI: 10.52396/JUSTC-2023-0156
JUSTC, **2024**, 54(X):

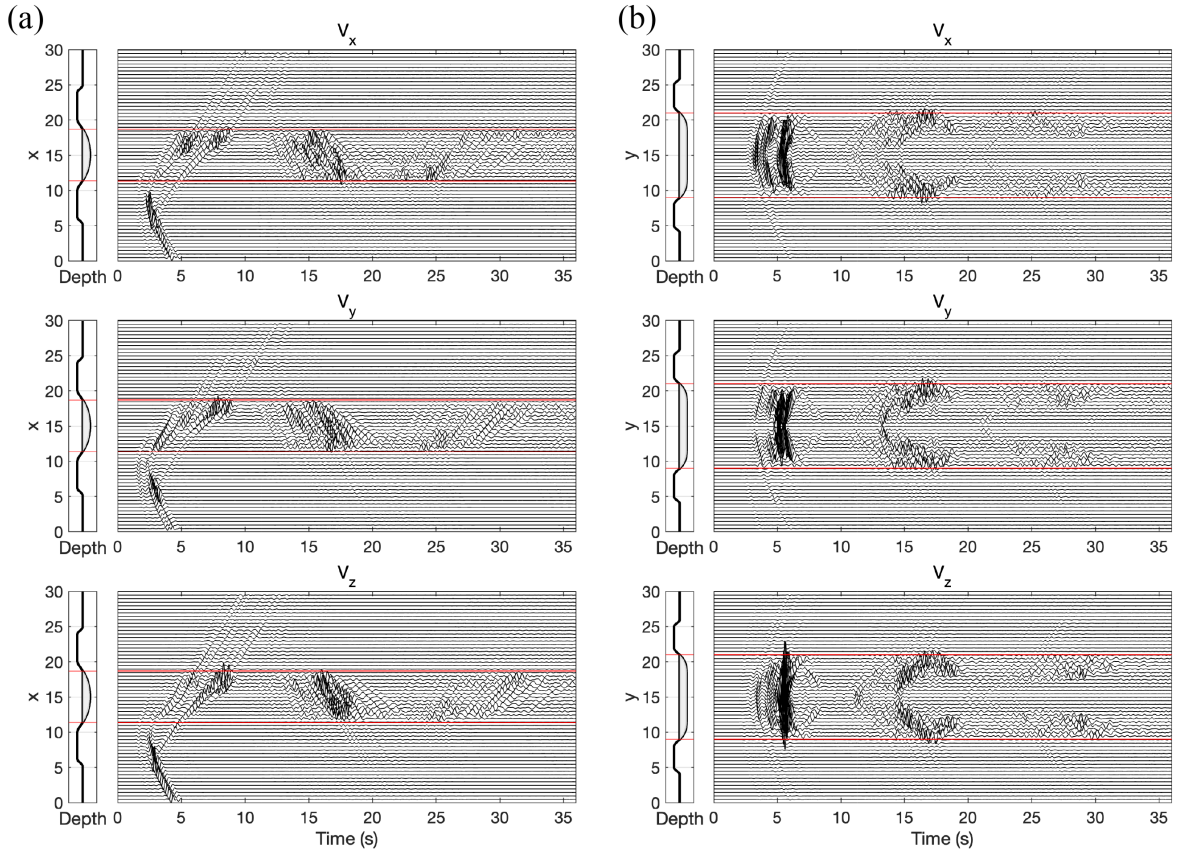

Fig. 4. 2-D section of model geometry and corresponding 3-component velocity seismograms for (a) receiver line 1 and (b) receiver line 2 in Fig. 3a with the fixed-depth baseline model.

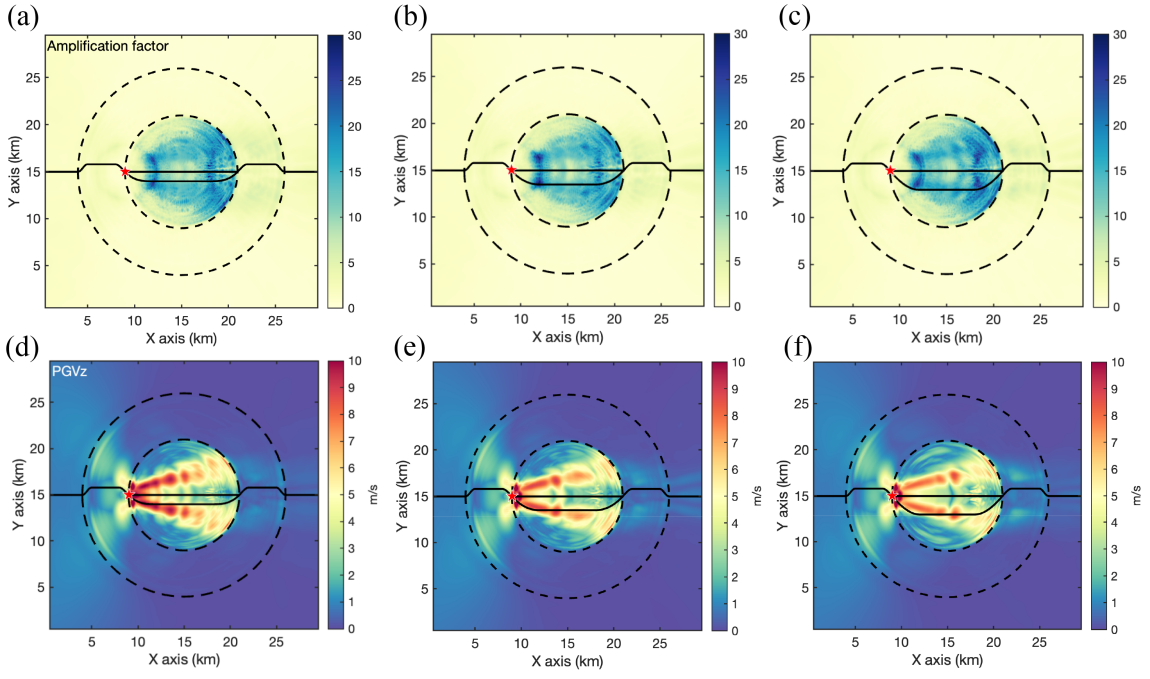

Fig. 5. Amplification factor of fixed-depth basin model with LVL depths of (a) 1000 m, (b) 1500 m, and (c) 2000 m, and corresponding vertical PGV (d), (e), (f). The dashed circle shows the boundary of LVL and topography.

DOI: 10.52396/JUSTC-2023-0156
JUSTC, **2024**, 54(X):

tiple reflections in the amplification components. In Fig. 6d, there is no velocity contrast in this model, the amplification is only caused by the tomography.

4 Discussion

Near-field ground motion amplification in basin areas has been the subject of extensive research through numerous 2D and 3D studies. However, in areas associated with sedimentary faults, the gradual rotation and subsidence of the fault's down-dropped block result in greater space by the fault, allowing for the deposition of thicker sedimentary layers. This leads to the formation of wedge-shaped sedimentary layers, usually observed in basin-rift structure regions [40]. The fault is typically located at the deeper end of the fault. To address this gap, we constructed a wedge-shaped basin model by introducing d_1 and d_2 (Fig. 1d). To maintain consistency in the model set-up, we retained the same seismic source configuration as in the previous model. In such a model configuration, we obtained the results as shown in Fig. 7b, 7d. d_1 = 3 000 m and d_2 = 1 500 m is applied in this case, whose definition is described in Fig. 1d.

For a model with wedge-shaped LVL, the general character of the wave propagation is similar to the fixed-depth basin model. Strong amplification still occurs on the far end of the basin compared to the other model. The model's results also exhibit some differences compared to the previous results with a fixed basin depth. According to the PGV distribution (Fig. 7a), the V-shaped feature within the basin area exhibits a more extended reach due to the basin, continuing into the transitional zone where it converges towards the ground at the far side of the basin. Its distribution is more continuous compared to a fixed-depth basin model. In terms of the amplification factor (Fig. 7b), the result shows that the amplification factor on the shallower side of the basin is higher than that on the corresponding position in the fixed-depth basin model. This discrepancy may be attributed to the fact that once waves enter the basin, the larger angle between the basin's bottom boundary and the wavefront weakens the multiple reflections of waves within the LVL. As the basin depth gradually becomes shallower, stronger amplification occurs on the far end of the basin.

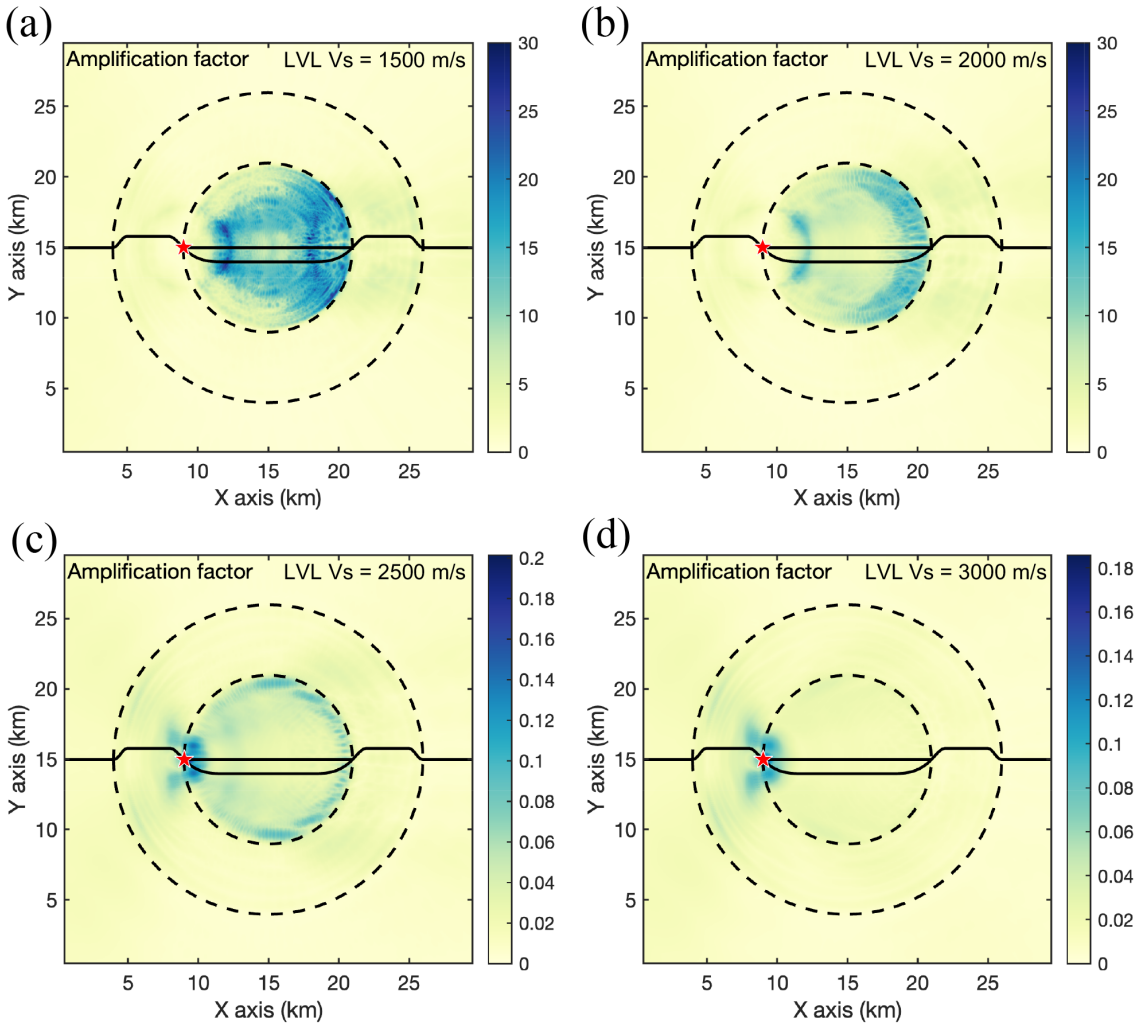

Fig. 6. Amplification factor of fixed-depth basin model with LVL velocities of (a) 1500 m/s, (b) 2000 m/s, (c) 2500 m/s, and (d) 3000 m/s, with a velocity of 3000 m/s of the bedrock.

DOI: 10.52396/JUSTC-2023-0156
JUSTC, **2024**, 54(X):

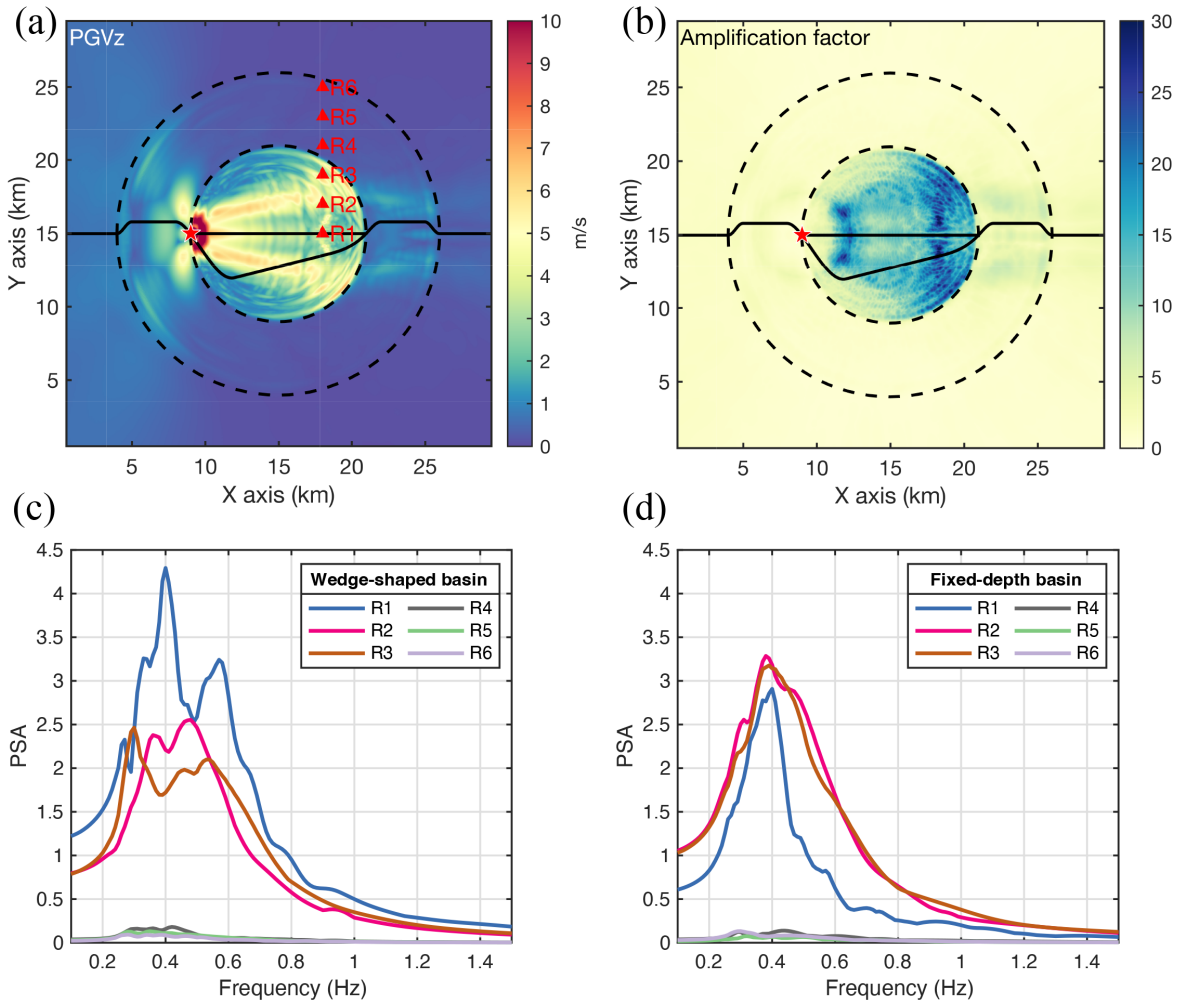

Fig. 7. (a) PGVz for wadge-shaped LVL model. (b) z-component Amplification factor of the wedged-shaped LVL model. (c) PSA with a 5% damping ratio of the wedge-shaped model at receivers in Figure 7a. (d) PSA with a 5% damping ratio of 1500 m fixed-depth basin model at corresponding receivers.

We compare the PSA of 6 receivers (Fig. 7a) between the wedge-shaped model and the 1500 m fixed-depth model (Fig. 7c). Among these 6 receivers, R4, R5, and R6 are located outside the basin area. The PSA at R2 and R3 of the wedge-shaped model is truncated and exhibits a transition from a single-peak distribution in the fixed-depth basin model to a double-peak distribution compared with the fixed-depth model. The PSA of R1 at the wedged-shape model has a larger peak than the fixed-depth model. The difference at R1 indicates that under the wedge-shaped basin, due to variations in the reflection characteristics on the boundary of the LVL, the amplification pattern differs from that of a fixed-depth basin. This illustrates the effect of basin geometries on the response of structures to ground motion. Furthermore, compared to receivers outside the basin, the PSA peaks of receivers within the LVL zone have slightly shifted towards higher frequencies. The PSA at receivers outside the LVL zone is nearly identical between the two models.

The wedge-shaped model is x-axis symmetric and the z-component PGV and the amplification factor both show a smaller value at the symmetry axis compared to the maximum of the area. Although the back-and-forth oscillations of seismic waves occur on the opposite sides of the basin, their ground motion at this location is weaker compared to its surroundings. This highlights the significance of model configuration for different ground motion characteristics. Compared to the LVL effect, the influence of the topography on ground motion is secondary, which coincides with the previous studies [23,41]. The amplification due to topography primarily exists at locations where there are variations in the terrain, notably evident at the edge of the western mountain range in Fig. 6d.

The current configuration places a seismic source near the outer boundary between the LVL and the underlying bedrock, under the assumption that a basin-rift structure can generate faults at the boundary. However, large earthquakes can also originate on faults adjacent to the basin. To investigate the impact of source location, we conducted additional tests with two different source positions outside the basin. Fig. 8 presents a comparison of the maximum amplification factor and z-component velocity snapshots for three different source locations S1, S2, and S3. The simulation region is extended to 40 km × 30 km × 12 km to adjust the change of source locations. The same focal mechanism and source depth are used. The x-axis coordinates of Source S1 remain at 9000 m, con-

DOI: 10.52396/JUSTC-2023-0156
JUSTC, **2024**, 54(X):

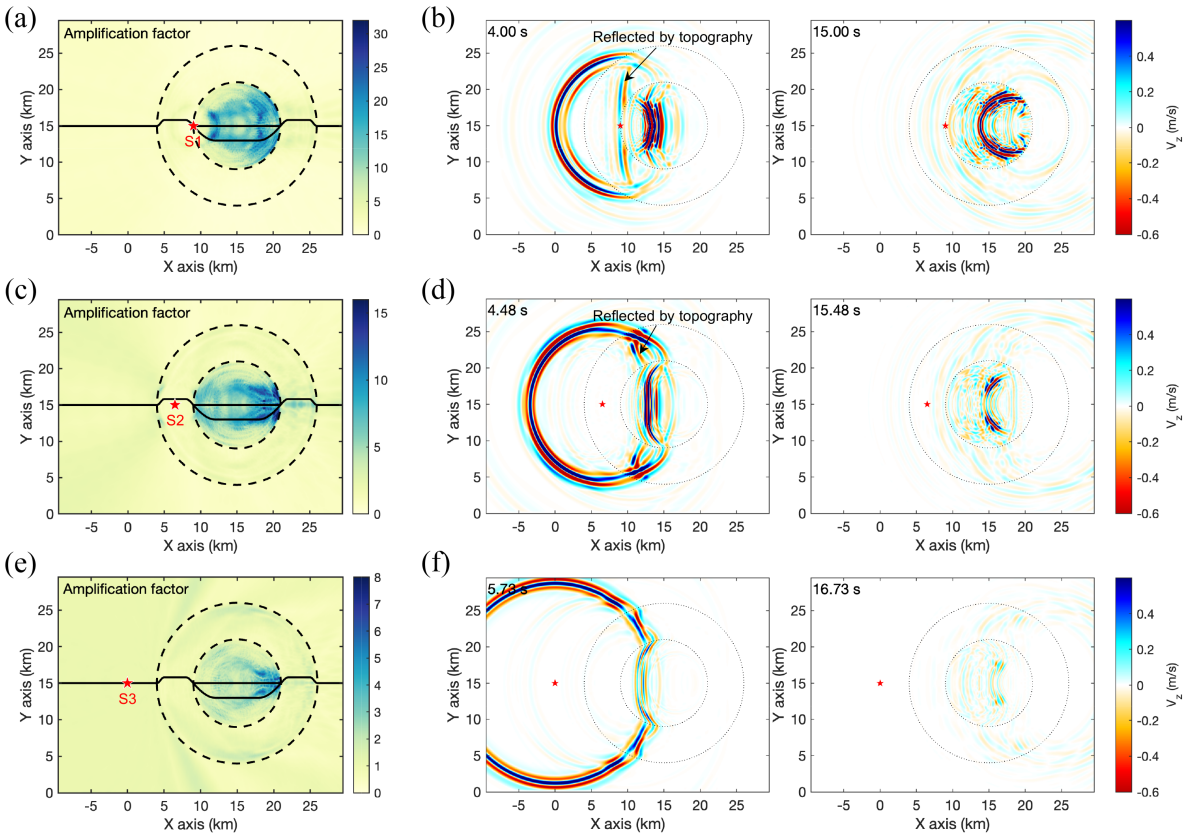

Fig. 8. Amplification factor with different source locations (Figures a, c, e) and corresponding z-component velocity snapshot at 4 s and 15 s after the wavefront reaching LVL (Figures b, d, f). The result is calculated using a fixed-depth basin model.

sistent with earlier models. However, for Source S2, we shifted its x-axis coordinate to 6500 m, placing it beneath the center of the surrounding mountains. Source S3 is moved further away from the mountain area, with its x-axis coordinate at 0 m. The basin depth is 2000 m and the LVL V_s velocity is 1500 m/s, compared to the bedrock V_s velocity of 3000 m/s.

The maximum amplification factor exhibits noticeable differences for different source locations, S1, S2, and S3 (Fig. 8a, 8c, 8e). As the distance between the source and the LVL increases, the maximum amplification factor decreases. This outcome is not surprising for two main reasons. Firstly, the energy entering the LVL diminishes with growing distance because of the attenuation and geometrical spreading. Secondly, considering a source depth of 1000 m and an LVL depth of 2000 m, waves entering the basin at greater distances exhibit a nearly perpendicular wavefront orientation to the Earth's surface, resulting in a reduction of multiple reflections within the LVL.

The results with different source distances consistently indicate a shift in the maximum amplification towards the far side of the basin from the source. To better understand this phenomenon, we present the z-component velocity snapshots in Fig. 8b, 8d, and 8f. The travel time from the source to the LVL for source models S1, S2, and S3 are approximately 0 s, 4.8 s, and 5.73 s, respectively. Thus, we choose the snapshot time at 4 s and 15 s after the wavefront reaches the LVL. For source models S1 and S2, the reflection of seismic waves induced by the mountain is observed. This reflected wave, upon entering the LVL, amplifies the amplitude and prolongs the duration of the ground motion within the LVL. For source model S2, seismic waves are trapped for a longer time because of the free-surface reflection. This leads to a larger amplification factor almost everywhere on the outside slope of the surrounding mountain. This finding aligns with previous research, both analytical and numerical, indicating that the amplification caused by the mountain topography typically occurs on the mountain ridges or slopes [23,33,41–43]. While the source is outside of the mountain region, the reflection of seismic wave amplitude is too subtle to discern. Nevertheless, once the wavefronts enter the basin area, they can still be trapped in the basin area and amplify the ground motion although the amplitude is weaker compared to previous models.

5 Conclusions

Scrutinizing the basin amplification effect is crucial to earthquake hazard assessment. To address the gap of the coupling effect of basin topography and low-velocity layer, we design several different basin models generated using a combination of a half-sine function and cubic spline interpolation, with different low-velocity sediments in it and simulate the seismic wave propagation using the finite difference method. Comparative analysis with results from a homogeneous half-space model allowed us to assess the influence of the low-velocity layer and topography on ground motion. Compared to the effect of basin topography, which mainly concentrates

DOI: 10.52396/JUSTC-2023-0156
JUSTC, **2024**, 54(X):

in the enclosing mountain area near the side facing toward the seismic source, the low-velocity layer effect is more crucial to determine the ground motion amplification. With a higher velocity contrast between the LVL and the bedrock, the stronger seismic amplification mainly appears in the central flat region of the basin and is more pronounced on the side of the basin opposite to the seismic source. With a lower velocity contrast, the ground motion amplification primarily occurs in the periphery part of the basin. In addition to the fixed-depth basin model, we also proposed a wedge-shaped basin model which is common in rift-basin structures, and compared the differences in PSA of the wedge-shaped and fixed-depth basin models. A stronger PSA is noticed at the point closer to the central line of the basin. The distance between the source and the basin, coupling with the basin boundary topography, can have a strong impact on the ground motion amplification. Our work provides useful insight into understanding the basin amplification patterns and helps to explain the near-field ground motion with various basin characteristics. It also highlights the importance of both velocity structure and topography in seismic hazard assessments.

Acknowledgements

This work is supported by the University of Science and Technology of China (USTC) Research Funds of the Double First-Class Initiative (YD2080002009), the National Natural Science Foundation of China (42074049, 41974042), and the Youth Innovation Promotion Association of the Chinese Academy of Sciences (2023471). All data used in this study are derived from numerical simulations. The figures are plotted using MATLAB. Numerical computations were performed on Hefei Advanced Computing Center.

Conflict of interest

The authors declare that they have no conflict of interest.

Biographies

Zeyu Lu is a master's student at University of Science and Technology of China. He received his bachelor's degree in Geophysics from China University of Geosciences (Beijing) in 2022. His research mainly focuses on the earthquake dynamic rupture process and earthquake ground motion simulation.

Feng Hu is an Associate Professor at University of Science and Technology of China (USTC). He received his Ph.D. degree in Geophysics at USTC in 2014. His research mainly focuses on rupture dynamics, earthquake hazard simulations, and seismicity analysis.

References

[1] Pitarka A, Irikura K, Iwata T, et al. Three-dimensional simulation of the near-fault ground motion for the 1995 Hyogo-Ken Nanbu (Kobe), Japan, earthquake. *Bulletin of the Seismological Society of America*, **1998**, *88* (2): 428–440.

[2] Yu Z, Liu Q, Xu J, et al. Simulation of dynamic rupture process and near-field strong ground motion for the Wenchuan earthquake. *Bulletin of the Seismological Society of America*, **2022**, *112* (6): 2828–2846.

[3] Graves R W. Preliminary analysis of long-period basin response in the Los Angeles region from the 1994 Northridge earthquake. *Geophysical Research Letters*, **1995**, *22* (2): 101–104.

[4] Xu W, Wu P, Li D, et al. Joint inversion of Rayleigh group and phase velocities for S-wave velocity structure of the 2021 Ms6.0 Luxian earthquake source area, China. *Earthquake Science*, **2023**, *36* (5): 356–375.

[5] Zhao Y, Jiang G, Lei X, et al. The 2021 Ms 6.0 Luxian (China) earthquake: Blind reverse-fault rupture in deep sedimentary formations likely induced by pressure perturbation from hydraulic fracturing. *Geophysical Research Letters*, **2023**, *50* (7): e2023GL103209.

[6] Bard P-Y, Bouchon M. The seismic response of sediment-filled valleys. Part 2. The case of incident P and SV waves. *Bulletin of the Seismological Society of America*, **1980**, *70* (5): 1921–1941.

[7] Dravinski M. Influence of interface depth upon strong ground motion. *Bulletin of the Seismological Society of America*, **1982**, *72* (2): 597–614.

[8] Dravinski M, Mossessian T K. Scattering of plane harmonic P, SV, and Rayleigh waves by dipping layers of arbitrary shape. *Bulletin of the Seismological Society of America*, **1987**, *77* (1): 212–235.

[9] Ayoubi P, Mohammadi K, Asimaki D. A systematic analysis of basin effects on surface ground motion. *Soil Dynamics and Earthquake Engineering*, **2021**, *141*: 106490.

[10] Kamal, Narayan J P. 3D basin-shape ratio effects on frequency content and spectral amplitudes of basin-generated surface waves and associated spatial ground motion amplification and differential ground motion. *Journal of Seismology*, **2015**, *19* (2): 293–316.

[11] Qin Y, Wang Y, Takenaka H, et al. Seismic ground motion amplification in a 3D sedimentary basin: the effect of the vertical velocity gradient. *Journal of Geophysics and Engineering*, **2012**, *9* (6): 761–772.

[12] Liu Z X, Huang Z E, Zhang Z, et al. Three-dimensional preconditioned FM-IBEM solution to broadband-frequency seismic wave scattering in a layered sedimentary basin. *Engineering Analysis with Boundary Elements*, **2021**, *133*: 1–18.

[13] Liu Z X, Huang Z E, Meng S B. Three-dimensional IBEM solution to seismic wave scattering by a near-fault sedimentary basin. *Engineering Analysis with Boundary Elements*, **2022**, *140*: 220–242.

[14] Wirth E A, Vidale J E, Frankel A D, et al. Source-dependent amplification of earthquake ground motions in deep sedimentary basins. *Geophysical Research Letters*, **2019**, *46* (12): 6443–6450.

[15] Frankel A, Stephenson W, Carver D. Sedimentary basin effects in Seattle, Washington: Ground-motion observations and 3D simulations. *Bulletin of the Seismological Society of America*, **2009**, *99* (3): 1579–1611.

[16] Frankel A D, Carver D L, Williams R A. Nonlinear and linear site response and basin effects in Seattle for the M 6.8 Nisqually, Washington, earthquake. *Bulletin of the Seismological Society of America*, **2002**, *92* (6): 2090–2109.

[17] Jayalakshmi S, Dhanya J, Raghukanth S T G, et al. 3D seismic wave amplification in the Indo-Gangetic basin from spectral element simulations. *Soil Dynamics and Earthquake Engineering*, **2020**, *129*: 105923.

[18] Esmaeilzadeh A, Motazedian D. Sensitivity analysis for finite-difference seismic basin modeling: A case study for Kinburn basin, Ottawa, Canada. *Bulletin of the Seismological Society of America*, **2019**, *109* (6): 2305–2324.

[19] Fu C, Gao M, Chen K. A study on long-period response spectrum of ground motion affected by basin structure of Beijing. *Acta Seismologica Sinica*, **2012**, *34* (03): 374–382. (in Chinese)

[20] Lee S-J, Chen H-W, Huang B-S. Simulations of strong ground motion and 3D amplification effect in the Taipei basin by using a composite grid finite-difference method. *Bulletin of the Seismological Society of America*, **2008**, *98* (3): 1229–1242.

[21] Miksat J, Wen K-L, Sokolov V, et al. Simulating the Taipei basin response by numerical modeling of wave propagation. *Bulletin of*

DOI: 10.52396/JUSTC-2023-0156
JUSTC, **2024**, 54(X):

Earthquake Engineering, **2010**, *8* (4): 847–858.
[22] Sokolov V, Wen K-L, Miksat J, et al. Analysis of Taipei basin response for earthquakes of various depths and locations using empirical data. *Terrestrial, Atmospheric and Oceanic Sciences: TAO*, **2009**, *20* (5): 687–702.
[23] Boore D M. A note on the effect of simple topography on seismic SH waves. *Bulletin of the Seismological Society of America*, **1972**, *62* (1): 275–284.
[24] Bouchon M. Effect of topography on surface motion. *Bulletin of the Seismological Society of America*, **1973**, *63* (2): 615–632.
[25] Davis L L, West L R. Observed effects of topography on ground motion. *Bulletin of the Seismological Society of America*, **1973**, *63* (1): 283–298.
[26] Çelebi M. Topographical and geological amplifications determined from strong-motion and aftershock records of the 3 March 1985 Chile earthquake. *Bulletin of the Seismological Society of America*, **1987**, *77* (4): 1147–1167.
[27] Geli L, Bard P-Y, Jullien B. The effect of topography on earthquake ground motion: A review and new results. *Bulletin of the Seismological Society of America*, **1988**, *78* (1): 42–63.
[28] Bourdeau C, Havenith H B. Site effects modelling applied to the slope affected by the Suusamyr earthquake (Kyrgyzstan, 1992). *Engineering Geology*, **2008**, *97* (3): 126–145.
[29] Rizzitano S, Cascone E, Biondi G. Coupling of topographic and stratigraphic effects on seismic response of slopes through 2D linear and equivalent linear analyses. *Soil Dynamics and Earthquake Engineering*, **2014**, *67*: 66–84.
[30] Luo Y, Fan X, Huang R, et al. Topographic and near-surface stratigraphic amplification of the seismic response of a mountain slope revealed by field monitoring and numerical simulations. *Engineering Geology*, **2020**, *271*: 105607.
[31] Huang D, Sun P, Jin F, et al. Topographic amplification of ground motions incorporating uncertainty in subsurface soils with extensive geological borehole data. *Soil Dynamics and Earthquake Engineering*, **2021**, *141*: 106441.
[32] Wang G, Du C Y, Huang D R, et al. Parametric models for 3D topographic amplification of ground motions considering subsurface soils. *Soil Dynamics and Earthquake Engineering*, **2018**, *115*: 41–54.
[33] Hailemikael S, Lenti L, Martino S, et al. Ground-motion amplification at the Colle di Roio ridge, central Italy: a combined effect of stratigraphy and topography. *Geophysical Journal International*, **2016**, *206* (1): 1–18.
[34] Zhang W, Zhang Z, Chen X. Three-dimensional elastic wave numerical modelling in the presence of surface topography by a collocated-grid finite-difference method on curvilinear grids. *Geophysical Journal International*, **2012**, *190* (1): 358–378.
[35] Hixon R. On increasing the accuracy of MacCormack schemes for aeroacoustic applications. In: 3rd AIAA/CEAS Aeroacoustics Conference. Reston, USA: American Institute of Aeronautics and Astronautics, **1997**.
[36] Chen X, Quan Y, Harris J M. Seismogram synthesis for radially layered media using the generalized reflection/transmission coefficients method; theory and applications to acoustic logging. *Geophysics*, **1996**, *61* (4): 1150–1159.
[37] Komatitsch D, Tromp J. Introduction to the spectral element method for three-dimensional seismic wave propagation. *Geophysical Journal International*, **1999**, *139* (3): 806–822.
[38] Brocher T M. Empirical relations between elastic wavespeeds and density in the Earth's crust. *Bulletin of the Seismological Society of America*, **2005**, *95* (6): 2081–2092.
[39] Wirth E A, Chang S W, Frankel A. 2018 report on incorporating sedimentary basin response into the design of tall buildings in Seattle, Washington. Reston, USA: U.S. Geological Survey, **2018**: Open-File Report 2018-1149.
[40] Withjack M O, Schlische R W, Olsen P E, et al. Rift-basin structure and its influence on sedimentary systems. In: Sedimentation in Continental Rifts. Claremore, USA: Society for Sedimentary Geology, **2002**: 57–81.
[41] Graizer V. Low-velocity zone and topography as a source of site amplification effect on Tarzana hill, California. *Soil Dynamics and Earthquake Engineering*, **2009**, *29* (2): 324–332.
[42] García-Pérez T, Ferreira A M G, Yáñez G, et al. Effects of topography and basins on seismic wave amplification: the Northern Chile coastal cliff and intramountainous basins. *Geophysical Journal International*, **2021**, *227* (2): 1143–1167.
[43] Lee S-J, Chan Y-C, Komatitsch D, et al. Effects of realistic surface topography on seismic ground motion in the Yangminshan region of Taiwan based upon the spectral-element method and LiDAR DTM. *Bulletin of the Seismological Society of America*, **2009**, *99* (2A): 681–693.

DOI: 10.52396/JUSTC-2023-0156
JUSTC, **2024**, 54(X):